

Mobilization of Colloidal Particles by Low-Frequency Dynamic Stress Stimulation

Richard E. Beckham, Amr I. Abdel-Fattah,* Peter M. Roberts, Reem Ibrahim, and Sowmitri Tarimala

Los Alamos National Laboratory, Los Alamos, New Mexico 87545

Received March 12, 2009. Revised Manuscript Received October 6, 2009

Naturally occurring seismic events and artificially generated low-frequency (1 to 500 Hz) elastic waves have been observed to alter the production rates of oil and water wells, sometimes increasing and sometimes decreasing production, and to influence the turbidity of surface and well water. The decreases in production are of particular concern, especially when artificially generated elastic waves are applied as a method for enhanced oil recovery. The exact conditions that result in a decrease in production remain unknown. Although the underlying environment is certainly complex, the observed increase in water well turbidity after natural seismic events suggests the existence of a mechanism that can affect both the subsurface flow paths and the mobilization of in situ colloidal particles. This article explores the macroscopic and microscopic effects of low-frequency dynamic stress stimulations on the release of colloidal particles from an analog core representing an infinitesimal section along the propagation paths of an elastic wave. Experiments on a column packed with 1 mm borosilicate beads and loaded with polystyrene microparticles demonstrate that axial mechanical stress oscillations enhance the mobilization of captured microparticles. Increasing the amplitude of the oscillations increases the number of microparticles released and can also result in cyclical spikes in effluent microparticle concentration during stimulation. Under a prolonged period of stimulation, the cyclical effluent spikes coincided with fluctuations in the column pressure data and continued at a diminished level after stimulation. This behavior can be attributed to rearrangements of the beads in the column, resulting in possible changes in the void space and/or tortuosity of the packing. Optical microscopy observations of the beads during low-frequency oscillations reveal that individual beads rotate, thereby rubbing against each other and scraping away portions of the adsorbed microparticles. These results support the theory that mechanical interactions between porous matrix grains are important mechanisms in flow path alteration and the mobilization of naturally occurring colloidal particles during elastic wave stimulation. These results also point to both continuous and discrete en masse releases of colloidal particles, perhaps because of circulation cells within the packing material.

Introduction

The effects of elastic waves—both naturally occurring and artificial—on the mobilization of colloidal particles and alteration of subsurface flow pathways are of concern for many applications including oil recovery, subsurface transport of contaminants, leakage of CO₂ geologic sequestration reservoirs, and remediation of contaminated aquifers. Natural seismic events and artificially induced elastic wave stimulations have been observed to alter oil well^{1,2} and water well³ production. In particular, artificially applied low-frequency elastic waves (≤ 500 Hz) have been studied extensively as a method for improving oil well production.^{1,4,5} Frequently, the results are positive with production increases of 20% or more during field studies in the oil and gas industries.^{1,4} On the laboratory scale, low-frequency elastic wave stimulation has been observed to increase substantially the removal of trichloroethylene, a dense nonaqueous phase liquid (DNAPL), from a sand pack⁶ and decane from sandstone.⁵ On some occasions, however, the application of low-frequency elastic

waves resulted in a decrease in the oil production rate in the field¹ and in the laboratory.⁵ Suggested mechanisms for enhanced well production under seismic stimulation (“seismic” in this article refers to all elastic stress waves in the earth, whether their source is natural or artificial) include improved percolation of oil due to the destruction of surface films in pores,² changes in the matrix wettability,⁵ shear of oil droplets due to the difference in the densities of water and oil,² and coalescence of oil droplets due to Bjerknes forces.² Although some or all of these mechanisms may be present in the subsurface to some extent during stimulation, they fail to include the role that the mobilization of in situ subpore-sized particles (colloids) plays in altering the formation permeability. This mechanism can lead to both advantageous and disadvantageous consequences in porous mass transport, depending on whether the mobilized colloids are expelled from the system or clog the pore throats further downstream. Currently, the relative roles of the numerous physical mechanisms underlying observed changes in well production due to the application of low-frequency dynamic stimulation remain to be fully determined.^{1,2,5,6}

The fact that seismic events can mobilize colloidal particles is evident in a study of drinking-water wells after the 2001 earthquake in Nisqually, Washington.³ As a result of this earthquake, a number of wells exhibited a marked increase in turbidity, some to the point of requiring redevelopment, as well as increases and decreases in flow.³ Similar observations have been recorded as a result of other earthquakes in different locations.⁷ The mobilization

*To whom correspondence should be addressed. E-mail: amr2450@lanl.gov.

(1) Roberts, P. M.; Esipov, I. B.; Majer, E. L. *Leading Edge* **2003**, *22*, 448–453.
(2) Beresnev, I. A.; Johnson, P. A. *Geophysics* **1994**, *59*, 1000–1017.
(3) Ballantyne, D.; Heubach, W. *The Nisqually, Washington, Earthquake of February 28, 2001*; ASCE Publications: Reston, VA, 2002; Chapter 4.
(4) Kostrov, S. A.; Wooden, W. O.; Roberts, P. M. *Oil Gas J.* **2001**, *99*, 47–55.
(5) Roberts, P. M.; Majer, E. L.; Lo, W. -C.; Sposito, G.; Daley, T. M. *Nonlinear Acoustics at the Beginning of the 21st Century*; MSU: Moscow, 2002.
(6) Roberts, P. M.; Sharma, A.; Uddameri, V.; Monagle, M.; Dale, D. E.; Steck, L. K. *Environ. Eng. Sci.* **2001**, *18*, 67–79.

(7) Elkhoury, J. E.; Brodsky, E. E.; Agnew, D. C. *Nature* **2006**, *441*, 1135–1138.

of in situ colloids can impact more than just water turbidity. Subsurface contaminant transport may occur because natural colloidal particles can act as carriers for highly sorbing and otherwise immiscible or insoluble contaminants such as nonaqueous phase liquids (NAPL) and actinide species.^{8,9} In addition to sorbing onto colloidal particles, NAPL droplets can also be stabilized by colloids through the formation of stable Pickering emulsions.¹⁰ It is conceivable that elastic waves could enhance the liberation of such contaminants, resulting in either the undesirable spread of the contaminants or the desirable recovery of the contaminants if coupled with a suitable groundwater remediation system.^{8,11} The reported enhanced liberation of colloidal particles during earthquakes is intriguing given that the natural seismic events were at a frequency lower than expected for the release of in situ colloidal particles.⁹ As is the case for changes in well performance, the mechanisms of colloidal particle release during seismic events are still largely unknown,⁹ but the distribution and mobility of colloids will certainly have major impacts on mass transport in any porous system. For example, migrating fines are known to clog some pore throats of the porous networks under appropriate conditions.^{9,12} If the enhanced liberation of colloids can be understood quantitatively, then the underlying mechanisms might be utilized in developing new techniques for enhanced oil recovery and subsurface remediation.

The effects of low-frequency (30–150 Hz) acoustic stimulation on colloidal particle transport in porous media have recently been investigated,⁸ where the colloidal dispersion, together with a conservative tracer, was injected into a laboratory column packed with glass beads during stimulation. The results indicated that low-frequency fluid pressure stimulation did reduce the average residence time of either the colloids or the conservative tracer in the column. The reduction in the colloidal particles' residence time was independent of their size and was maximized at the lowest frequency employed (30 Hz). The study, however, did not investigate the effect of acoustic stimulation on the mobilization of previously captured colloidal particles nor did it include mechanical stress coupled to the solid pore matrix as the dominant mode of stimulation. Other studies⁶ found that the mobilization of dense NAPL (DNAPL) pools can be enhanced by low-frequency stress oscillations. Similar studies on aqueous tracers found that solute transport increased with decreasing acoustic frequency¹³ and increasing acoustic intensity.¹⁴ In previous laboratory studies,^{5,6,9,11} low-frequency dynamic stress stimulation was observed to enhance the mobilization of NAPL and naturally occurring colloids in consolidated sandstone and unconsolidated sand. Curiously, dynamic stress stimulation not only enhanced the mobilization but also resulted in cyclical spikes in the effluent concentrations of both the colloids¹⁵ and NAPL⁶ when the levels of stimulation were sufficiently high. Although these spikes may at first appear to be random noise, their consistent behavior and uniform timing are sufficient to believe otherwise. These cyclical

spikes can provide valuable insight into the mechanisms coupling dynamic stress stimulations and mass transport in porous media and thus the mechanisms underlying enhanced oil well production under seismic stimulation. Unfortunately, current theory fails to provide an explanation for these observed cyclical spikes or the coupling mechanisms. The work presented here has two main objectives: (1) to determine if the effluent concentration spikes are an artifact resulting from the use of natural granular materials or if they are present when an idealized unconsolidated glass bead medium is used and (2) to identify potential colloidal particle release mechanisms during low-frequency elastic wave stimulation that explain the effluent concentration behavior.

Experimental and Analytical Procedures

Column experiments were conducted using the Dynamic Core Flow Stimulation System (DCFSS).⁶ The DCFSS holds the core material in a horizontal Viton sleeve surrounded by a confining fluid. The Viton sleeve is equipped with inlet and outlet ports allowing fluids to be pumped through the core and differential pressure gauges attached to ports along the length of the sleeve to measure changes in pore fluid pressure. Static radial and axial confinement stresses were applied to the sample to simulate realistic stress conditions in the earth and to achieve a sufficient fluid seal between the core sample and the Viton sleeve. Dynamic stress stimulations with a sinusoidal waveform were induced by a mechanical actuator (Etrema Terfenol-D magnetostrictive actuator) in contact with the fluid outlet end of the packed core. The mode of stimulation was mechanical stress/strain applied directly to the solid packed beads in the axial direction, as opposed to direct coupling to the flowing pore fluid pressure.

The current experiments used an artificial porous core composed of a 2.54-cm-diameter by 30-cm-long Teflon screen packed with 1 mm nominal diameter borosilicate glass beads. The sample was inserted into the DCFSS and confined at 2.4 MPa radial and 1.7 MPa axial static pressures. A vacuum was applied for 2 days to remove as much air as possible. Then the core was saturated under vacuum with deionized ultrapure water at neutral pH 7, and the total pore volume was determined to be approximately 60 mL. The core was then flushed with 18 L of the same water at a constant flow rate of 12 mL/h, during which the permeability was determined to be $20 \mu\text{m}^2$. Axial stress/strain measurements were acquired for the water-saturated core using a load cell in series with the mechanical actuator and a linear variable displacement transducer (LVDT) attached to the end of the core sample. These data were used to measure the Young's modulus (the ratio of stress to strain) of the bulk sample at different static and dynamic stress levels. Next, the core was injected at the same flow rate of 12 mL/h with a 1 L suspension of 2.26- μm -diameter fluorescent polystyrene (fPS) microparticles (Duke Scientific product number G0220) in ultrapure water at neutral pH 7. The number concentration of the fPS microparticles in the injected suspension was measured by flow cytometry to be approximately 1.7×10^6 particles/cm³. The microparticles had a density of 1.05 g/cm³ and were negatively charged at pH 7 because of sulfate groups at the end of the polymers. The ζ potential of the microparticles at pH 7 was measured to be -44 mV (Figure 1) using a Malvern Zetasizer 3000 HS. Throughout the loading process, the effluent microparticle concentration was monitored to ensure that (1) breakthrough was achieved and (2) the effluent microparticle concentration had stabilized. At the end of microparticle loading, the effluent microparticle concentration was approximately 1.1×10^6 particles/cm³. During all experimental stages described in this article, the flow rate through the column was maintained at 12 mL/h using a pulse-free pump (Quizix QX-6000) upstream of the column, resulting in an average linear velocity of 1.022 mm/min. The core was maintained in a horizontal position throughout the experiments.

The stimulation times varied but were on the order of hours. Although a natural seismic event would not last for such a long

(8) Thomas, J. M.; Chrysikopoulos, C. V. *J. Colloid Interface Sci.* **2007**, *308*, 200–207.

(9) Roberts, P. M. *Acoust. Phys.* **2005**, *51*, S140–S148.

(10) Tarimala, S.; Dai, L. L. *Langmuir* **2004**, *20*, 2492–2494.

(11) Roberts, P. M.; Abdel-Fattah, A. I. *Innovations in Nonlinear Acoustics: 17th International Symposium on Nonlinear Acoustics*; American Institute of Physics: Melville, NY, 2006.

(12) Santamarina, J. C.; Valdes, J. R.; Palmino, A. M.; Alvarellos, J. *IUTAM Proceedings on Physicochemical and Electromechanical Interactions in Porous Media*; Springer: Dordrecht, The Netherlands, 2005.

(13) Vogler, E. T.; Chrysikopoulos, C. V. *Geophys. Res. Lett.* **2002**, *29*, 5–1 to 5–4.

(14) Cherskiy, N. V.; Tsarev, V. P.; Konovalov, V. M.; Kuznetsov, O. L. *Trans. USSR. Acad. Sci.* **1977**, *232*, 201–204 (earth science sections).

(15) Roberts, P. M.; Abdel-Fattah, A. I. *Earth Planet. Sci. Lett.* **2009**, *284*, 538–543.

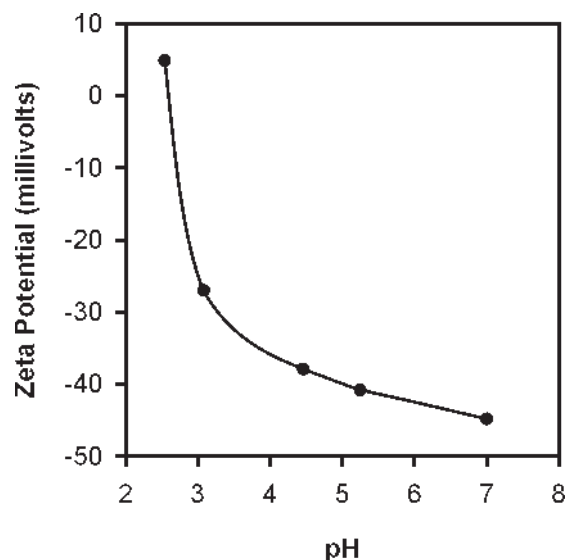


Figure 1. Zeta potential of 2.26 μm fluorescent polystyrene microparticles (Duke Scientific product number G0220) in water at varying pH levels as measured on a Malvern Zetasizer 3000 HS.

time, it is common for artificial seismic sources to be applied for days or weeks during field tests where low-frequency elastic waves have been investigated for use in enhanced oil recovery. More importantly, conducting the experiment for this extended length of time allowed the temporal form of the effluent particle count curve to be determined, thereby providing valuable information about the kinetics of the particle release mechanism.

Effluent samples of 6 mL volume were collected every 30 min using an automatic fraction collector (Isco Foxy Junior). Samples were collected in polyethylene tubes treated with a trace amount of sodium dodecylsulfate (SDS) to minimize the coagulation of the microparticles and their deposition onto the tube walls. The samples were capped after collection and stored at 4 °C until analysis. Immediately prior to analysis, the samples were again treated with SDS and then subjected to sonication in a laboratory ultrasonic bath. These steps were determined from a set of separate experiments and were found to be necessary and sufficient for the complete recovery of the microparticles in the sample tubes. Number concentrations of microparticles in the effluent samples were measured using a Partec PAS III flow cytometer. The flow cytometer was used in fluorescence mode to discriminate between the injected microparticles and any possible colloidal contaminants.

To gain insight into the pore-scale behavior of the microparticles, microscopic visualization experiments were conducted to confirm that the microparticles would adsorb onto the surfaces of the glass beads under the conditions of column loading and to identify the likely mechanism of microparticle release as a result of dynamic stimulation. The pore-scale experiments were conducted in cells fabricated by sandwiching randomly packed 1 mm borosilicate glass beads (identical to those used in the column experiments) between two glass microscope slides (Figure 2). The cells were equipped with inlet and outlet ports, sealed with epoxy, thoroughly flushed with deionized ultrapure water at neutral pH 7, and then placed horizontally on the stage of an upright optical microscope. An aliquot from the same polystyrene microparticles/ultrapure water dispersion used in the core experiments was injected into the cells using a low-flow syringe pump (Harvard Apparatus pump 33). The flow rate was adjusted to produce an average linear velocity in the cells of 1.022 mm/min, equivalent to that used in the core experiments. Two sets of pore-scale experiments were performed. In the first, the cell was injected with just enough microparticle dispersion to fill the cell completely, the inlet and outlet of the cell were closed, and the cell was allowed to

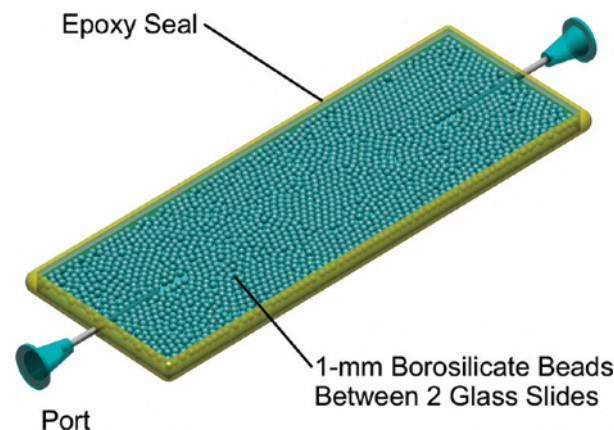


Figure 2. Rendering of the pore-scale experimental cell design.

equilibrate overnight. In the second set, the microparticle dispersion was continuously injected into the cell for 17 h, followed by continuous flushing with deionized ultrapure water at neutral pH 7 for 92 h. The cell was then subjected to two different types of stimulation: (1) low-frequency oscillatory flow induced by manual actuation of the injection syringe and (2) an ultrasonic field created by an ultrasonic transducer placed on the outer surface of the cell and driven by a sinusoidal function generator and rf amplifier. The purpose of the first stimulation was to replicate the dynamic stress stimulation conditions of the core experiments, and that of the second was to explore the effects of exciting complete sonic waves in the cell. Fluorescent images of the individual and collective glass beads were collected before, during, and after stimulation using the Automated Video Microscopic Imaging and Data Acquisition System (AVMIDAS).¹⁶

To interpret the results from the column experiments, the effluent particle concentration, column pressure, and confining fluid temperature data were examined using continuous wavelet transforms (CWT) to capture the presence of periodicities and waves at specific frequencies.¹⁷ Compared to Fourier transform analysis, the CWT possesses the advantage of being able to detect waves that are transient in nature.¹⁷ The CWT is defined as

$$W(a, b) = \frac{1}{\sqrt{a}} \int_{-\infty}^{\infty} f(x) \psi^*\left(\frac{x-b}{a}\right) dx \quad (1)$$

where $W(a, b)$ is the CWT, a is the scaling factor, b is the position parameter, $f(x)$ is the data or signal, x is the independent variable of the data, and $\psi^*(x)$ is the wavelet.¹⁷ The scaling factor controls the size, and thus the wavelength, of the wavelet.¹⁷ Given the discrete nature of the data reported in this paper, the CWT was implemented accordingly,

$$W(a, b) = \frac{1}{\sqrt{a}} \sum_{n=1}^N C_n \psi^*\left(\frac{n-b}{a}\right) \quad (2)$$

where n is the data index, N is the total number of data points, and C is the concentration, temperature, or pressure data. The wavelet used to analyze the data was the Haar wavelet, which is defined as¹⁷

$$\psi(t) = \begin{cases} 1 & \text{for } 0 \leq t < \frac{1}{2} \\ -1 & \text{for } \frac{1}{2} \leq t < 1 \\ 0 & \text{otherwise} \end{cases} \quad (3)$$

(16) Abdel-Fattah, A. I.; Roberts, P. M. *Innovations in Nonlinear Acoustics: 17th International Symposium on Nonlinear Acoustics*; American Institute of Physics: Melville, NY, 2006.

(17) Stark, H.-G. *Wavelets and Signal Processing. An Application-Based Introduction*; Springer: The Netherlands, 2005.

Results

Core-Scale Experiments. The mechanical behavior of the saturated core is depicted in Figure 3. The behavior of the Young's modulus (stress/strain ratio) in response to dynamic stress shows a marked change in the 100 to 150 kPa rms stress amplitude range. This observation indicates a threshold-type behavior where a change in the nonlinear stress/strain response of the bead pack occurs above certain stress amplitudes.

The normalized particle breakthrough curves, $C/C_o(t)$, and associated continuous wavelet transforms (CWT) for the three dynamic stress stimulation episodes are shown in Figures 4–6. In these Figures, $C(t)$ is the effluent microparticle number concentration at any given time, t , and C_o is the effluent microparticle concentration prior to stimulation, which was calculated by averaging about 20 effluent samples prior to stimulation and was found to be approximately 292, 194, and 142 particles/cm³ for the first, second, and third stimulation episodes, respectively. Also provided are the fractions of remaining particles released from the column, determined by mass balance calculations of cumulative numbers of particles injected and released from the column prior to the start of each stimulation episode.

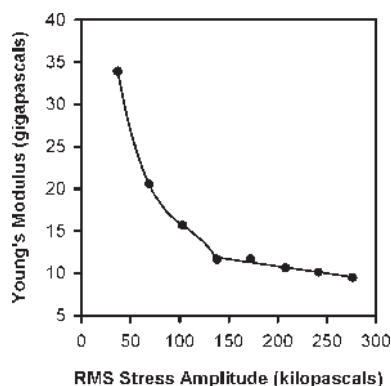


Figure 3. Young's modulus data for the flooded glass bead pack in the DCFSS column prior to loading with colloidal particles.

Figure 4 shows the results of the first dynamic stress stimulation episode (90.5 h duration, 26 Hz frequency, and 200 kPa rms stress amplitude). At the start of stimulation, $C/C_o(t)$ spiked at 7.4 before dropping and spiking again to approximately 11.75. These two spikes are manifested in the CWT as distinctive V-shaped features. The width of the first spike is five samples (150 min). Because of its range, this spike is believed to be due to an actual concentration spike in the collected samples. Random noise (e.g., an isolated miscounting of a sample by the flow cytometer or a contaminated sample) would have a range of only one sample. Also, the samples were analyzed in random order as determined by a random number generator in a spreadsheet. As a result, longer-term errors introduced by instrument drift would appear in the data as discontinuities with ranges of one or two samples. After the second spike, $C/C_o(t)$ decays exponentially, consistent with first-order release kinetics. A few spikes in $C/C_o(t)$ are also observed during this exponential decay. However, these few spikes are weak and infrequent and do not appear to occur at any regular interval that would suggest cyclic behavior. $C/C_o(t)$ continued to decay after stimulation ceased, reaching a stabilized value of approximately 0.53. The column pressure was observed to cycle through a 24 h pattern that closely matched the background temperature variations measured in the column and the laboratory. Thus, these apparent pressure cycles were caused by room temperature influencing the gain of the pressure transducers. Any actual pressure changes in the column due to stimulation were below the level of detection during this first episode.

Figure 5 shows the results of the second dynamic stress stimulation episode (5.5 h duration, 26 Hz frequency, and 350 kPa rms stress amplitude). During stimulation, the effluent microparticle concentration demonstrated an increasing trend, occurring in three distinct spikes, to a maximum value of approximately $140C_o$ immediately prior to the end of stimulation. This maximum value is more than 1 order of magnitude higher than the maximum $C/C_o(t)$ value observed in the previous episode and is due to the higher rms stress amplitude applied. As before, the range of each spike seen in this episode is on the order of four to five samples (120 to 150 min), and the presence of the spikes is noted by three distinctive V-shaped features in the CWT. At the

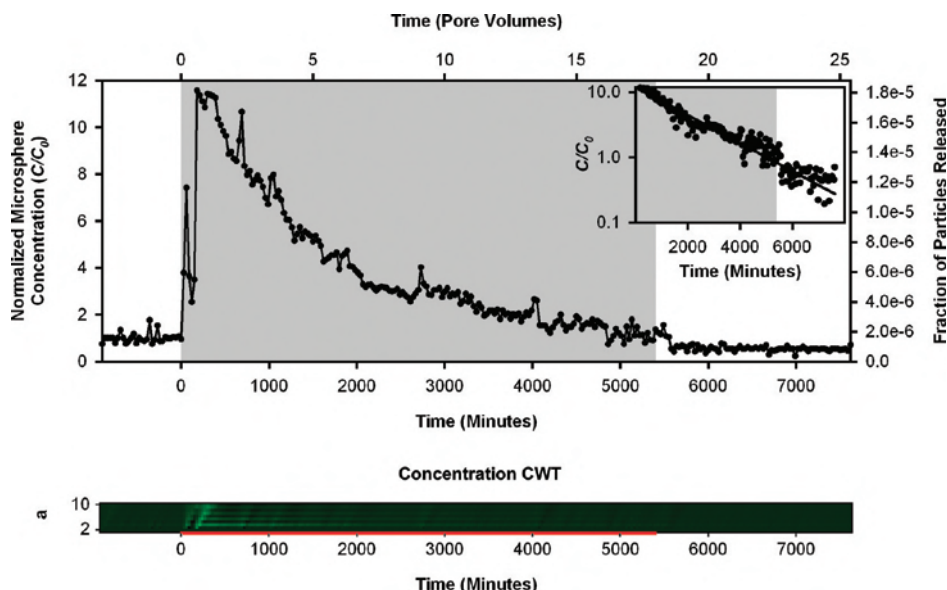


Figure 4. Normalized effluent microparticle concentration data (top, dotted line) and wavelet transform (bottom) for the first dynamic stress stimulation episode at 26 Hz frequency and 200 kPa amplitude. Time (t) = 0, the shaded background, and the red horizontal line indicate the start of the stimulation and its duration. The concentration data are also plotted on a semilogarithmic scale (inset, dots) from the start of stimulation, with an exponential decay curve (inset, line) fit to the data by rms error minimization.

end of the stimulation, the concentration dropped to approximately $0.73C_0$. No additional effluent concentration spikes, outside of random noise, are observed in the data. Likewise, there are no

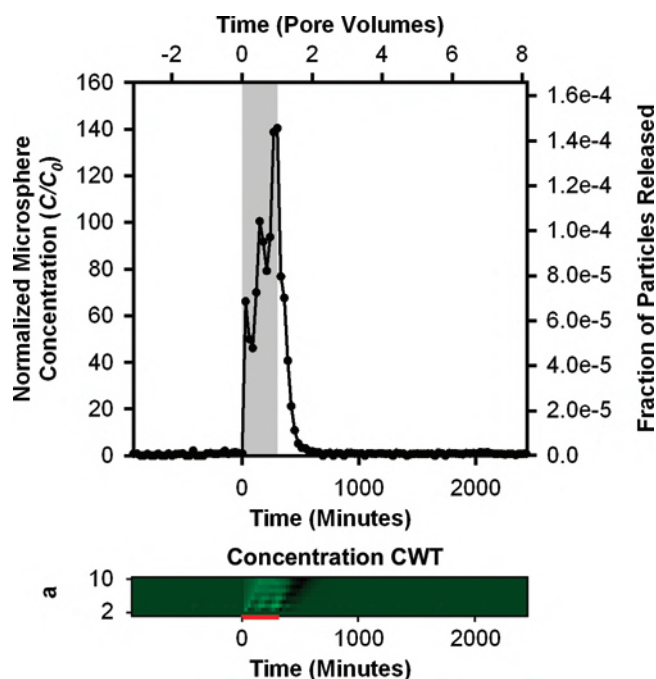


Figure 5. Normalized effluent microparticle concentration data (top, dotted line) and wavelet transform (bottom) for the second dynamic stress stimulation episode at 26 Hz frequency and 350 kPa amplitude. Time (t) = 0, the shaded background, and the red horizontal line indicate the start of stimulation and its duration.

additional V-shaped features present in the CWT. As was observed during the first episode, the pressure data correlated strongly with the room-temperature data, and any actual pressure changes in the column due to stimulation were below the level of detection.

Figure 6 shows the results of the third dynamic stress stimulation episode, where the applied rms stress amplitude was the same (350 kPa) as in the second episode but the duration was increased to 25.5 h. Shortly after the start of stimulation, the effluent concentration increased to a maximum of approximately $63C_0$ and then followed an exponentially decaying trend throughout the remainder of the stimulation. Superimposed on the exponential decay are a series of distinct concentration spikes separated by an average interval of 5.875 samples (176 min), visible as a series of V-shaped features in the CWT. Surprisingly, these spikes continued to occur, but with diminished intensity, at regular intervals for 78 samples (39 h) after stimulation was stopped. They then dampened out as the effluent concentration stabilized at approximately $0.85C_0$. Concentration spikes were not observed before the stimulation was applied.

Figure 7 shows the temperature and pressure data along with the associated CWTs for the third episode. The data in this Figure have been normalized using the following equations

$$P_{\text{normalized}} = \frac{P - P_{\min}}{P_{\max} - P_{\min}} \quad (4)$$

$$T_{\text{normalized}} = \frac{T - T_{\min}}{T_{\max} - T_{\min}} \quad (5)$$

where $P_{\min} = -2.59$ kPa, $P_{\max} = -0.412$ kPa, $T_{\min} = 22.3$ °C, and $T_{\max} = 29.5$ °C are the minimum and maximum pressures and temperatures, respectively, observed over the entire time span

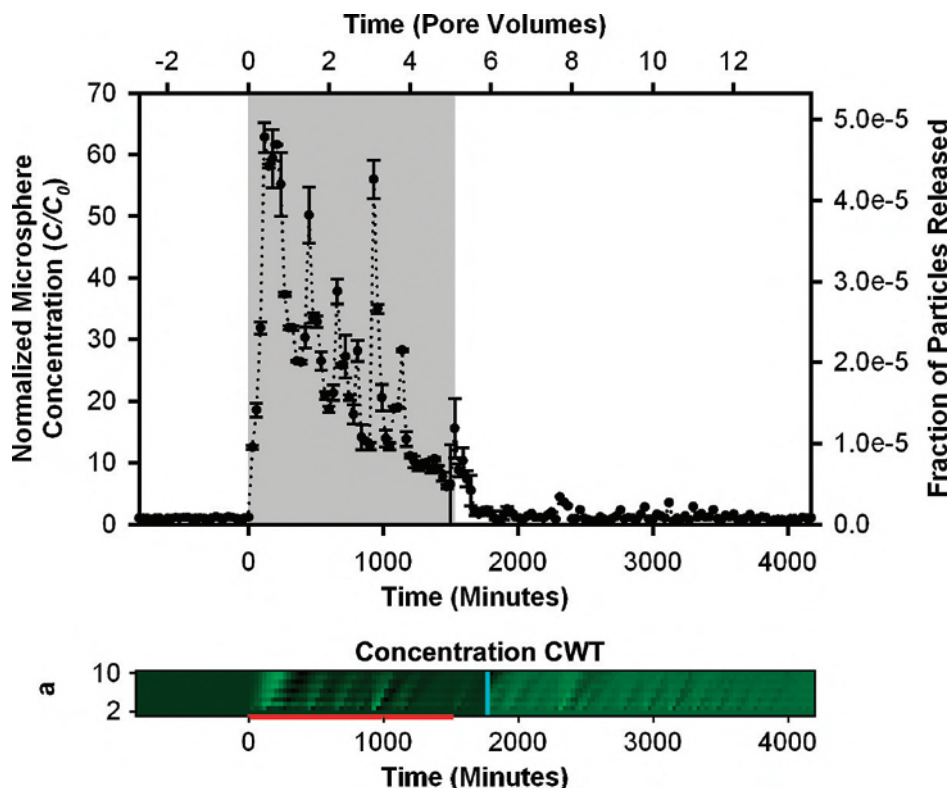


Figure 6. Normalized effluent microparticle concentration data points and averages with error bars (top) and wavelet transform (bottom) for the third dynamic stress stimulation episode at 26 Hz frequency and 350 kPa amplitude. Time (t) = 0, the shaded background, and the red horizontal line indicate the start of stimulation and its duration. The contrast and brightness of the CWT is enhanced to the right of the blue line.

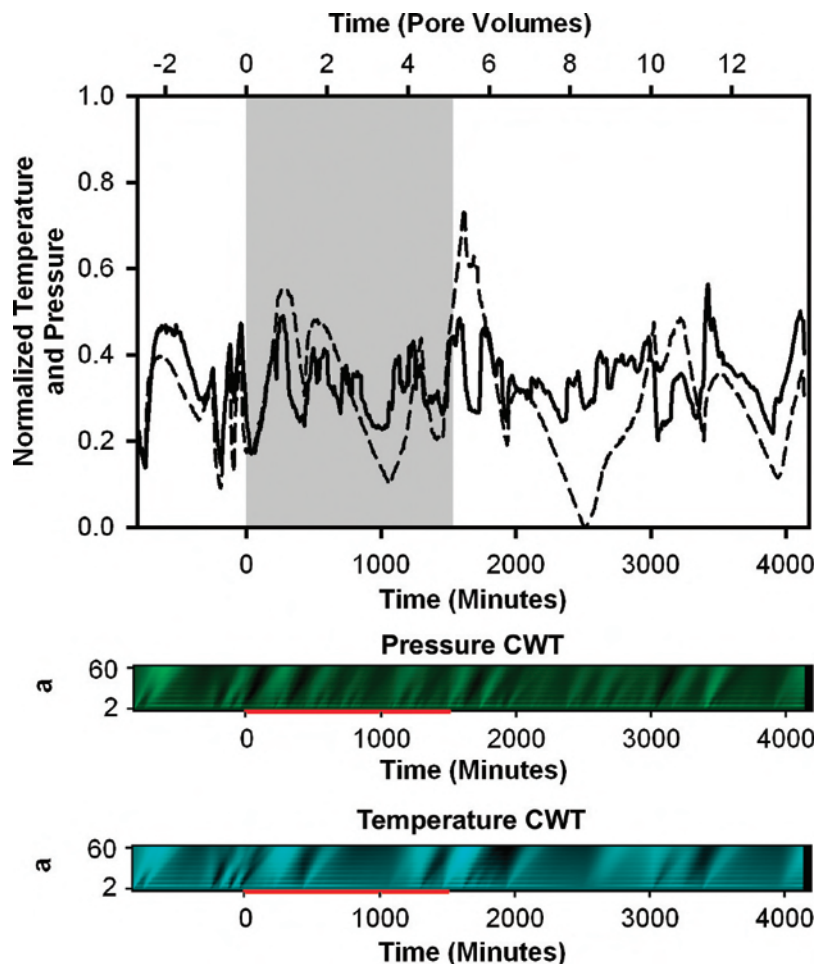


Figure 7. Normalized column pressure data (top, solid line), confining vessel internal temperature (top, dashed line), and corresponding CWTs for the third dynamic stress stimulation episode at 26 Hz frequency and 350 kPa amplitude. Time (t) = 0, the shaded background, and the red horizontal line indicate the start of stimulation and its duration.

of the stimulation experiments. Notice that prior to stimulation the pressure data correlate strongly with the background temperature data. Both data sets display the same 24 h pattern observed during the previous two stimulation episodes. Thus, the pressure data fluctuations prior to stimulation are again due to temperature-induced transducer gain variations and do not represent actual pressure changes within the column. During stimulation, however, the pressure fluctuations begin to deviate significantly from the behavior of the temperature data. This loss of correlation was not observed during the previous two episodes and indicates the appearance of actual pressure changes within the column. Initially, the 24 h pressure pattern becomes unstable (at about $t = 300$ min). By the time the stimulation is stopped, the pressure and temperature data are completely uncorrelated. This persists until around $t = 3000$ min, at which point the original 24 h correlation cycle is restored. The onset of pressure instability, loss of correlation, and recovery to background conditions can all be seen clearly in the pressure and temperature CWTs. The pressure data CWT demonstrates that the instabilities occur with approximately the same periodicity as the $C/C_0(t)$ spikes seen in Figure 6 and cease at approximately the same time.

Pore-Scale Experiments. In the initial pore-scale experiment, where the fPS microparticles dispersed in ultrapure water were allowed to equilibrate in the absence of flow, the microparticles were observed to settle to the bottom of the cell without adsorbing onto the surface of the glass beads. At first, the microparticles were uniformly distributed throughout the cell

and exhibited random thermal motion. Overnight the microparticles settled and adsorbed onto the cell's bottom surface, and no microparticles were observed to adsorb onto the surface of the glass beads.

In the subsequent pore-scale experiment, where the microparticle dispersion was continuously injected through the cell, a significant number of microparticles adsorbed onto the surfaces of the glass beads and the cell's bottom surface. Continuous flushing with ultrapure water at the same flow rate as that of injection did not cause any observable changes in the beads' surface coverage. The microparticles coated the glass beads, and the degree of coverage decreased from the inlet to the outlet, indicating that more sites on the beads' surfaces were still available for adsorption in the cell's outlet region. While continuing experiments prevented the disassembly of the packed beads column and inspection of the beads, the results of the second pore-scale episode indicate that the microparticles adsorbed onto the glass beads in the column, where loading occurred under continuous flow. Given that both the microparticles and glass beads are negatively charged under the current chemical conditions (deionized water, pH ~ 7), the above pore-scale observations point to an increased collision efficiency between the microparticles and the beads caused by flow through the cell, resulting in significant microparticle adsorption onto the surface of the beads.

Low-frequency flow oscillations caused the glass beads to shift and rotate, rubbing their surfaces together. Evidence of microparticle

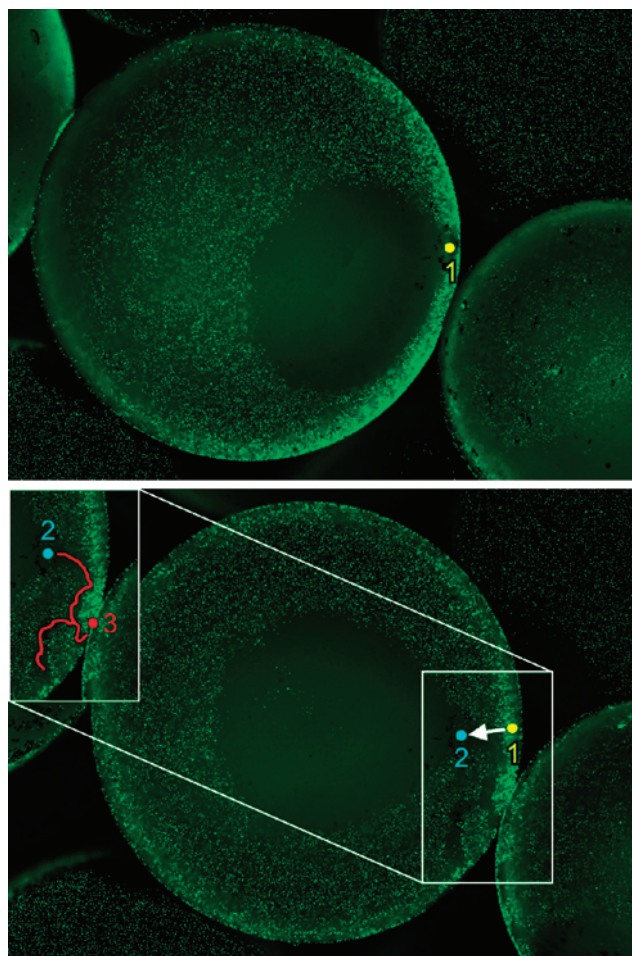


Figure 8. Fluorescent images captured at 50 \times magnification of glass beads coated with fPS microparticles after continuous loading followed by flushing with ultrapure water. Images captured before (top) and after (bottom) an episode of low-frequency flow oscillations. A distinctive patch at location 1 in the top image rotates to location 2 in the bottom image. The inset highlights a path on the surface of the bead scraped clean by contact during rotation with a neighboring bead. Location 3 in the inset is the approximate point of contact when the bottom image was captured.

scraping and displacement on the beads' surfaces when beads rub against each other is given in Figure 8, and that when beads rub against the cell walls is given in Figure 9. In Figure 8, a distinctive patch at location 1 in the top image is observed to move to location 2 in the bottom image. The inset highlights a path scraped clear of microparticles by rubbing against a neighboring bead, where location 3 in the inset is the approximate point of contact when the bottom image was captured. In Figure 9, the scraping of the bead against the cell wall is observed to generate two piles of microparticles in front of the point of contact. The inset in the top image highlights the areas cleared of microparticles by the contact, as does the inset in the bottom image, where the wide blue marks indicate two new areas cleared of microparticles during the capturing of the top and bottom images.

Finally, acoustic stimulation of the pore-scale cell at different ultrasonic frequencies did not cause scraping of the adsorbed microparticles, and the grinding of beads against each other or the cell walls was not observed. The ultrasonic stimulations were only able to move some beads that were not in tight contact with their neighbors or the cell walls, causing them to hit neighboring beads and the top and bottom surfaces of the cell.

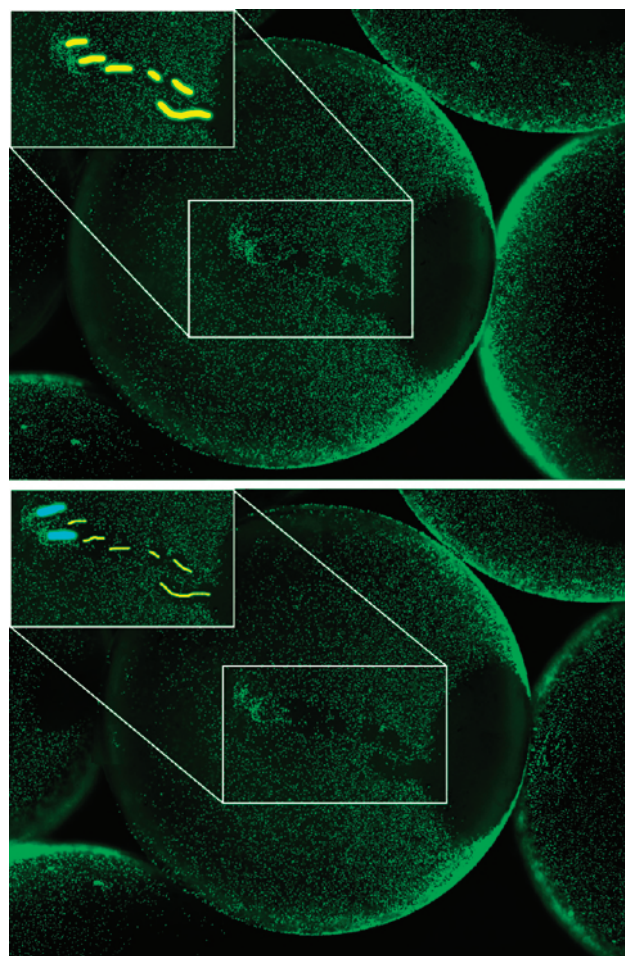


Figure 9. Fluorescent images captured at 50 \times magnification of glass beads coated with fPS microparticles after continuous loading, followed by flushing with ultrapure water. Images captured before (top) and after (bottom) an episode of low-frequency flow oscillations. These two images provide evidence of the beads scraping against the cell wall during oscillations as well as the piling up of particles in front of the point of contact. The insets highlight the locations of the paths scraped clear, with the yellow marks indicating areas scraped before the top image was captured and blue marks in the bottom image showing new areas scraped after the top image was captured.

Discussion

The core-scale experiments demonstrate that low-frequency stimulation mobilizes captured microparticles whose diameters are much smaller than the wavelength of stimulation. The microparticle effluent concentration behavior during stimulation points to at least two distinct microparticle release mechanisms. One release mechanism is responsible for the uniform exponential decay in $C(t)$, and another is responsible for the distinct spikes at higher stress amplitude. The sudden drop in the exponential decay behavior of $C/C_0(t)$ shortly after ceasing stimulations depicted in Figures 4 and 6 indicates that the first mechanism operates only during stimulations. The continuation of concentration spikes after ceasing stimulations in Figure 6, however, indicates that the second mechanism operates during and after the dynamic stress stimulations. The exponential decay is attributed to the first-order release kinetics of the microparticles from the glass bead surfaces that is relatively uniform throughout the bead pack.¹⁵ The pore-scale experimental observations (Figures 8 and 9) suggest that this relatively uniform microparticle release is due to the localized

grinding of the beads that is expected to take place among the majority of the beads throughout the pack. The distinct concentration spikes, however, can be attributed to simultaneous rearrangements of multiple grains producing discrete en masse releases of adsorbed microparticles. These simultaneous rearrangements can be explained by the formation of circulation cells that consist of multiple grains rotating as a rigid mass during compaction of the bead pack. These circulation cells have been documented in the literature¹⁸ to take place in granular material and are evident by our preliminary discrete element modeling (DEM)¹⁹ results shown in Figure 10. It has been suggested that these cells develop because of buckling of the particle force chains.¹⁸

The abrupt incidents of circulation cells in the packed bead column resulting in a discrete, en masse release of particles is consistent with the erratic pressure data coinciding with the discrete microparticle releases during the third stimulation episode (Figures 6 and 7). If these circulation cells occur during stimulation, in other words, during compaction of the glass bead pack, then it can be argued that they are also likely present during poststimulation, in other words, during the slow relaxation of the compacted bead pack. Thus, the presence of circulation cells can explain the continued discrete microparticle release after stimulation. Additional evidence of these circulation cells stems from the observed sudden change in the Young's modulus behavior in Figure 3. This sudden change is likely associated with the activation of a new mechanical interaction mechanism between individual beads, which can in turn be attributed to the development of circulation cells within the column. Figure 3 indicates that the activation of this mechanism occurs above a given stress amplitude threshold in the 100 to 150 kPa range. However, the discrete, en masse release of particles was distinguishable only during the core-scale column experiments at stress amplitudes above 200 kPa. This small discrepancy can be explained by the fact that, as indicated by the axial column length data, the column was more compact during the stimulation episodes reported here than during the initial stress/strain data collection. We expect that column compaction increases the Young's modulus and hence the stress amplitude required to initiate circulation cells.

Identical behavior of distinct spikes in column effluent concentrations and thus in the en masse releases was observed for naturally occurring colloids¹⁵ and NAPL⁶ during and after low-frequency dynamic stress stimulations of sandstone and irregularly shaped natural sand, respectively. As a result, the behavior of the column in the current experiments cannot be attributed to the idealized shape of the current packing or its noncohesive nature. Circulation cells are not anticipated in cohesive materials such as sandstone. However, microfracturing due to transgranular and intergranular fractures and grain deformation, sliding, and rotation mechanisms have been documented in the literature^{20,21} to occur during stressing and compaction weakening of sandstone and are likely to produce similar effects and result in discrete en masse releases of adsorbed microparticles or NAPL in these systems. Further research is planned to confirm the presence of these mechanisms.

Modeling. To simulate the column effluent concentration behavior during the second and third stimulation episodes (Figures 5 and 6), the overall behavior was broken down into those behaviors expected from the two mechanisms discussed

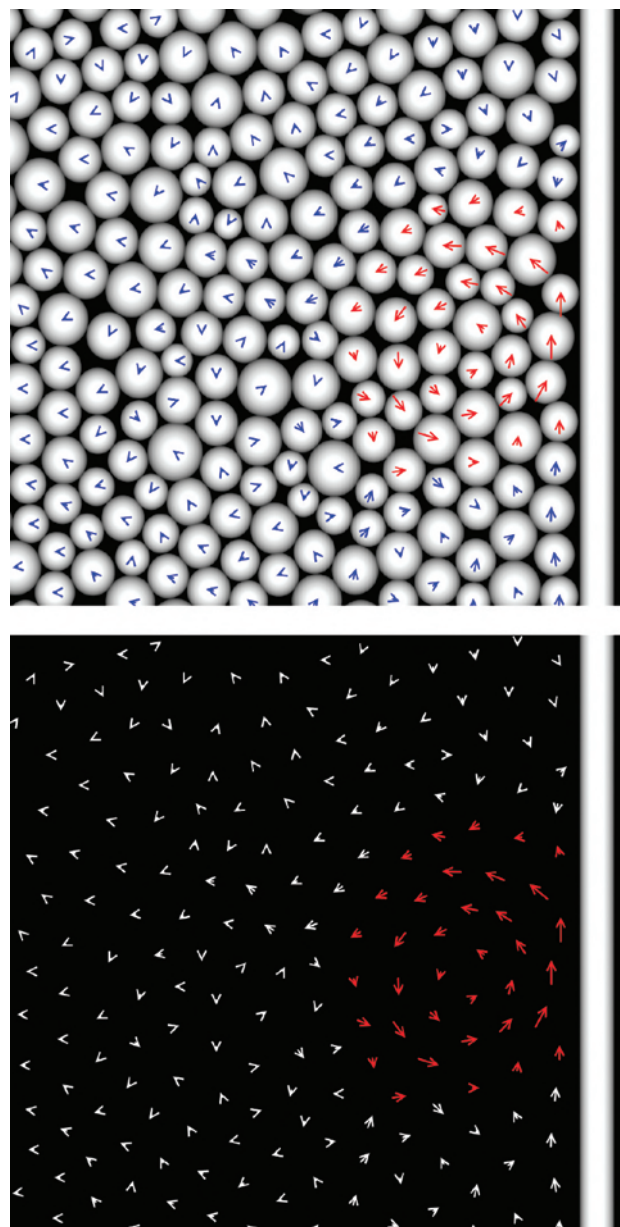


Figure 10. Preliminary discrete element model results of a confined, polydisperse granular material under compaction, illustrating the presence of a circulation cell. The arrowheads indicate the grains' directions of travel over several thousand time steps, and the arrow tails plot the initial and final positions of the grains over the time span of interest. The arrows are superimposed onto the grains in their final positions (top) to illustrate the grains' relative diameters and are provided without the grains (bottom) for clarity. The circulation cell is indicated by the use of red arrows.

above. The first mechanism (i.e., first-order microparticle release kinetics) can be described by the simple exponential decay function

$$P1_n = a \exp(-bn) \quad (6)$$

where n is the sample number, $P1_n$ is the total microparticle count contained in sample n due to the localized grinding release mechanism, and a and b are constants representing the initial jump in microparticles concentration and the decay rate constant, respectively. Equation 6 was fit to the data minima between the concentration spikes in Figure 6, resulting in values of $a = 2969.5$

(18) Rege, N. V. *Computational Modeling of Granular Materials*; Massachusetts Institute of Technology: Cambridge, MA, 1996, 152.

(19) Cundall, P. A.; Strack, O. D. L. *Geotechnique* **1979**, *29*, 47–65.

(20) Sayers, C. M.; Schutjens, P. M. T. M. *Leading Edge* **2007**, *5*, 597–601.

(21) Schutjens, P. M. T. M.; Ruig, H. d. *Phys. Chem. Earth* **1997**, *22*, 97–103.

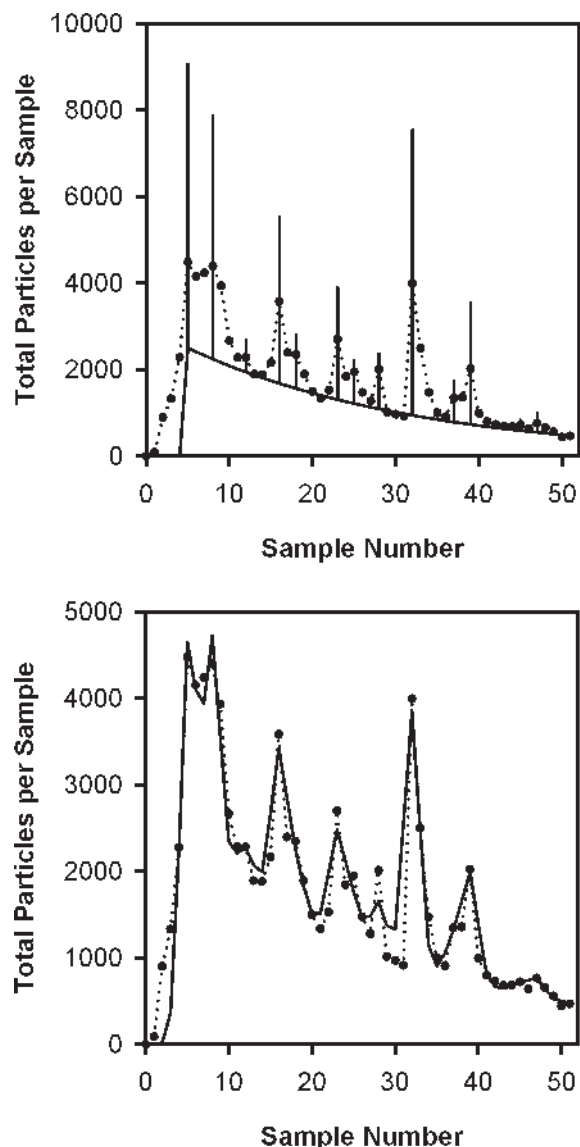


Figure 11. Comparison of experimental data and model. The data from the third stimulation episode (top and bottom, points and dotted line) can be modeled by an exponential decay fit to the data minima plus discrete concentration spikes (top, solid lines). Convoluting the decay and spikes with a Gaussian function to simulate diffusion and multiple flow pathways within the column (bottom, solid line) provides a good fit between the simulation results and experimental data.

and $b = 0.035$. Prior to sample five (the maximum of the first data spike), $P1_n$ was assumed to be zero.

The total particle count due to the discrete, en masse releases ($P2_n$) was then added to $P1_n$. $P2_n$ was assumed to be zero everywhere except for sample numbers that coincide with actual and apparent spike maxima in Figure 6 ($n = 5, 8, 12, 16, 18, 23, 25, 28, 32, 37, 39, 45$, and 47). To simulate the advective-diffusive

transport of the microparticles in the column, the summation was then convolved with a Gaussian function

$$TP_n = \frac{1}{N} \sum_{i=-5}^5 \left\{ (P1_{n+i} + P2_{n+i}) \exp \left[\frac{-(i^2)}{\lambda} \right] \right\} \quad (7)$$

where TP_n is the total particle count in sample n , N is a normalization constant, and λ controls the width of the Gaussian function. N was determined accordingly:

$$N = \sum_{i=-5}^5 \exp \left[\frac{-(i^2)}{\lambda} \right] \quad (8)$$

Fitting the model to the data required the determination of values for λ and $P2_n$. Using a simple Monte Carlo algorithm coded in FORTRAN that minimized the rms error between the experimental data and the model, it was determined that $\lambda = 1.66$ and $P2_n = 6568, 5633, 758, 3858, 1233, 2588, 1003, 1277, 6600, 957, 2797, 243$, and 460 at $n = 5, 8, 12, 16, 18, 23, 25, 28, 32, 37, 39, 45$, and 47 , respectively. The top graph in Figure 11 provides the experimental data from the third episode during stimulation expressed in terms of total particles per sample, along with the exponential curve fit to the data minima and the modeled concentration spikes ($P1_n + P2_n$). The bottom graph compares the convolved model (TP_n) with the experimental data. The Pearson product moment correlation coefficient between the data and the convolved model equals 0.952, indicating the excellent agreement of the simulations with the experimental data.

Conclusions

The low-frequency mechanical stimulation of a glass-bead-packed column mobilized adsorbed microparticles whose diameters are orders of magnitude less than the wavelength of stimulation. The most plausible release mechanisms appear to be associated with the compaction and relaxation of the granular material that result in the scraping of the grain surfaces, thereby mechanically displacing the adsorbed microparticles. The results of past studies suggest that similar compaction/surface scraping-based mechanisms are also present in natural granular and cohesive materials. Although further research is needed to confirm the presence of these mechanisms, this study supports the hypothesis that the changes in oil and water well production often observed during and after seismic events may be due in part to the release of natural colloids. This can cause either beneficial or harmful effects on formation permeability, depending on whether the released particles are expelled from the porous matrix or cause subsequent downstream fouling of flow pathways. The results of this study suggest that any event resulting in the compaction of an oil-bearing formation—seismic or otherwise, including a reduction in pore pressure due to oil recovery—may reduce the production rate if the formation has a low permeability and a high natural colloid concentration.

Acknowledgment. This work was funded by the U.S. Department of Energy Basic Energy Sciences Program under the Los Alamos National Laboratory contract no. DE-AC52-06NA25396.